BIOENGINEERING

Implantable microcoils for intracortical magnetic stimulation

Seung Woo Lee,[1,2] Florian Fallegger,[3] Bernard D. F. Casse,[3] Shelley I. Fried[1,2]*

2016 © The Authors, some rights reserved; exclusive licensee American Association for the Advancement of Science. Distributed under a Creative Commons Attribution NonCommercial License 4.0 (CC BY-NC).

Neural prostheses that stimulate the neocortex have the potential to treat a wide range of neurological disorders. However, the efficacy of electrode-based implants remains limited, with persistent challenges that include an inability to create precise patterns of neural activity as well as difficulties in maintaining response consistency over time. These problems arise from fundamental limitations of electrodes as well as their susceptibility to implantation and have proven difficult to overcome. Magnetic stimulation can address many of these limitations, but coils small enough to be implanted into the cortex were not thought strong enough to activate neurons. We describe a new microcoil design and demonstrate its effectiveness for both activating cortical neurons and driving behavioral responses. The stimulation of cortical pyramidal neurons in brain slices in vitro was reliable and could be confined to spatially narrow regions (<60 μm). The spatially asymmetric fields arising from the coil helped to avoid the simultaneous activation of passing axons. In vivo implantation was safe and resulted in consistent and predictable behavioral responses. The high permeability of magnetic fields to biological substances may yield another important advantage because it suggests that encapsulation and other adverse effects of implantation will not diminish coil performance over time, as happens to electrodes. These findings suggest that a coil-based implant might be a useful alternative to existing electrode-based devices. The enhanced selectivity of microcoil-based magnetic stimulation will be especially useful for visual prostheses as well as for many brain-computer interface applications that require precise activation of the cortex.

INTRODUCTION

Neural prostheses that can reliably and effectively activate the cortex have the potential to treat a wide range of neurological and psychiatric disorders (*1*–*4*). However, effective activation is difficult, given the large diversity of cell types within the cortex coupled with an inability to selectively target (or avoid) individual types. Further, passing axons from neurons located in distant parts of the brain are highly sensitive to prosthetic stimulation (*5*); this can lead to the spread of activation well beyond the local region surrounding a given electrode and further diminish the ability to create precise patterns of neural activity (*6*–*8*). Maintaining response consistency over time with implanted electrodes has also been proven to be challenging (*1*, *9*, *10*). For example, electrodes implanted into the primary visual cortex (V1) of macaque monkeys each reliably elicited a visual percept (phosphene) shortly after implantation, but individual electrodes lost effectiveness within a few months (*9*). Although larger groupings of electrodes could be used to generate phosphenes, the need to couple electrodes together represents a significant loss in potential visual acuity. Although the factors underlying this loss in performance are not fully known, implantation into the cortex is known to induce a foreign body response that can include inflammation as well as other adverse biological reactions. The formation of glial scarring around individual electrodes (*11*, *12*) can alter or even block the electric fields induced by the stimulus with a change (or even loss) of the resultant neural response. Although increases to the amplitude of stimulation can sometimes be used to re-elicit some behavioral responses, the associated increase in power usage is detrimental, especially to devices intended for long-term implantation.

Magnetic stimulation from implantable microcoils offers several potential advantages over conventional electrode-based stimulation. For example, unlike the fields arising from electrodes, the electric fields that arise from magnetic stimulation are spatially asymmetric and can therefore be harnessed to selectively activate some neuronal subpopulations while simultaneously avoiding others (*13*, *14*). In the cortex, this could include, for example, the ability to activate vertically oriented pyramidal neurons (PNs) without activating horizontally oriented passing axons. Another potential advantage of microcoils is that unlike the electric fields initiated by electrodes, magnetic fields pass readily through biological materials, and therefore their efficacy will not be diminished, even by severe encapsulation. A third advantage is that the lack of direct contact between the metal coil and neural tissue makes coil-based stimulation less prone to the numerous problems that can arise at the brain-electrode interface (*10*, *11*, *15*, *16*), for example, the damage to the electrode and/or the surrounding tissue that can arise from delivery of high levels of charge. Further, coils can be completely insulated with soft biocompatible materials that have been shown to mitigate the cortical response to implantation (*17*, *18*).

Although the potential benefits of magnetic stimulation have been known for a long time, it was generally thought that coils small enough to be implanted into the cortex could not generate fields that were strong enough to modulate neuronal activity. Several years ago, Bonmassar *et al.* (*13*) showed that a commercial inductor, 500 μm in diameter and 1 mm long, could modulate activity of central nervous system neurons. They further showed that the field asymmetries from the inductor could be exploited to selectively activate some types of neurons while simultaneously avoiding others. Although this was encouraging, the cross-sectional profile of the inductor used in their study was still nearly 100× that of commonly used implants, thereby raising concerns about the ability to implant safely into the cortex. Nevertheless, the ability to activate neurons with small coils raised the possibility that even further reductions in coil size might be achievable. New, more efficient designs might also help to reduce the power levels associated with microcoils, which, despite some reduction since the original study, remain well above the levels associated with electric stimulation.

[1]Boston Veterans Affairs Healthcare System, Boston, MA 02130, USA. [2]Department of Neurosurgery, Massachusetts General Hospital, Harvard Medical School, Boston, MA 02114, USA. [3]Palo Alto Research Center, a Xerox company, Palo Alto, CA 94304, USA.
*Corresponding author. Email: Fried.Shelley@mgh.harvard.edu

Here, to explore the viability of coils small enough to be safely implanted, we first developed a computational model that allowed us to rapidly assess the potential effectiveness of new designs. We found that simple bends of microwires could generate fields that exceeded the known thresholds for neuronal activation. Fabricated prototypes were comparable in size to existing electrode implants and therefore, in addition to in vitro testing, could be safely implanted into the cortex for in vivo evaluation of their ability to drive neural circuits. Our results strongly support the viability of implantable microcoils as an attractive alternative to conventional electrode implants.

RESULTS

Computational modeling of microcoils

To better understand whether coils that are small enough to be implanted can activate cortical neurons, we modeled the fields arising from a single loop of the inductor used in previous microcoil studies (*13*, *14*, *19*). The dimensions of the loop were 500 μm × 500 μm, and the wire thickness was 10 μm (Fig. 1A, left). After deriving the magnetic and electric fields that arose from the single loop (Materials and Methods), we calculated the gradient of the electric field along three orthogonal dimensions; the strength of the gradient along the length of a neuron or axon is known to underlie activation (*5*, *20*), so surface plots that displayed the field gradient across the region surrounding the coil (Fig. 1A, middle) could be used to quickly assess potential effectiveness. We were especially interested in the component of the gradient oriented normal to the cortical surface (*dEx*/*dx* using the axes of Fig. 1), because this represents the driving force for activation of vertically oriented PNs. Whereas the peak amplitude of the stimulus current through the coil in previous studies could exceed 1 A, here we found that an amplitude of 1 mA produced a peak field gradient of ~50,000 V/m^2 (Fig. 1A, right), a value well above the 11,000-V/m^2 threshold previously reported for stimulation of peripheral axons with a transcranial magnetic stimulation coil (*21*). This therefore suggests that even a single loop of appropriately aligned coil could be effective for activating PNs. The spatial extent over which the peak field exceeded the threshold extended for only ~75 μm from the coil (Fig. 1A, top right) and therefore suggests that activation could be confined to only a few nearby cells. For the orientation of the coil in Fig. 1A, the component of the gradient that was parallel to the passing axons of layers 1 and 4 (*dEz*/*dz*) was 0 V/m^2 (Fig. 1A, bottom right), suggesting that those axons or similarly oriented processes would not be activated.

The coil shown in Fig. 1A is still considerably larger than existing cortical implants, so we explored whether even smaller designs could also generate suprathreshold fields and gradients. Consistent with electromagnetic theory, the peaks in *dEx*/*dx* were localized to the corners of the coil, that is, the regions containing sharp bends in the flow of current, and therefore we considered the possibility that even a single sharp bend of a wire might generate fields and gradients strong enough for activation. Accordingly, we considered the design of Fig. 1B (left, red thick trace). The 100-μm width of this coil would fit within a single cortical column and would be comparable in size to existing electrode implants, suggesting that it could be implanted safely into the cortex. The peak strength of the field gradient calculated for this coil was 49 kV/m^2 (Fig. 1B, middle and right panels), almost identical to that of the larger single loop; the spatial extent over which the gradient exceeded the threshold for the 1-mA stimulus was again narrowly confined, extending only ~60 μm.

Although the spatially narrow regions of activation estimated in Fig. 1 are highly attractive for applications in which focal activation is required, it is well established that prolonged implantation into the cortex induces a foreign body response that can lead to the formation of a high-impedance glial sheath around the implant with a resultant increase in distance to targeted neurons (*11*, *12*). Migration of neurons away from the implant can also occur as part of the foreign body response (*22*), and migration distances of ~75 μm were reported even for implants that did not deliver stimulation. The increased distance to viable neurons raises the possibility that the spatially narrow fields and gradients arising from low-amplitude stimuli may not extend far enough for the coil to remain effective following prolonged implantation. We therefore examined how the spatial extent of the induced fields and gradients was altered by changes to the amplitude of stimulation. We started by more closely examining the profiles of fields and gradients for the same 1-mA stimulus used in Fig. 1. One-dimensional plots of fields and vertical gradients (*dEx*/*dx*) were generated for multiple sections through the coil in both the vertical and horizontal directions (Fig. 2, A and B, respectively; the red dashed line in each plot of gradients represents the previously reported threshold level of 11,000 V/m^2). The portions of the trace in which the gradient exceeds the threshold provide an estimate of the approximate extent over which activation would occur. Because activation will be limited to only those regions that are external to the coil perimeter, we restricted our focus to the region to the left of the blue dotted line in Fig. 2A and outside the two blue dotted vertical lines in Fig. 2B. With this approach, the extracted portion of *dEx*/*dx* along the *x* axis is plotted in Fig. 2C (black) for a 1-mA stimulus, whereas the relevant portion of *dEx*/*dx* along the *y* axis is plotted in Fig. 2D (black). We performed a similar analysis for larger stimulus amplitudes (10, 25, 50, and 100 mA) and overlaid the corresponding traces (red, blue, green, and pink, respectively). Comparison of the individual plots reveals not only that the suprathreshold region increases with amplitude but also that it is asymmetric in the *x* and *y* directions; for example, for an amplitude of 100 mA, the suprathreshold region extends ~151 μm along the *x* axis and 414 μm along the *y* axis. To better visualize the full extent of this region, we developed a two-dimensional contour plot for all amplitudes (Fig. 2E). The plots confirm the sensitivity of this region to changes in amplitude as well as the relatively wide spatial extent over which the field gradient is suprathreshold for higher stimulus amplitudes. Note that even the largest stimulus amplitude used in Fig. 2 is well below the levels used in the original in vitro (*13*) and in vivo studies (*23*). Thus, the model results suggest that implanted microcoils will be able to effectively activate neurons over a spatially extensive region, for example, beyond the extent over which gliosis and cellular migration occur. Because magnetic fields pass readily through even high-impedance materials, the ability of implanted coils to reach these more distant regions may not be adversely affected, even by severe gliosis, the way that they can with electrodes.

Fabrication of microcoil probes and in vitro experiments

To verify that the new microcoils could activate cortical neurons, we microfabricated the coil design of Fig. 1B for use in physiological experiments (Materials and Methods; Fig. 3A). The coil consisted of a copper trace (10 μm wide × 2 μm thick) on a silicon substrate that had a cross-sectional area of 50 μm × 100 μm and a length of 2000 μm. The coil assembly had a dc resistance of ~15 ohms and was insulated with 300 nm of SiO_2 (Materials and Methods) to prevent the leakage of electric current into the tissue. A second, similarly sized microcoil

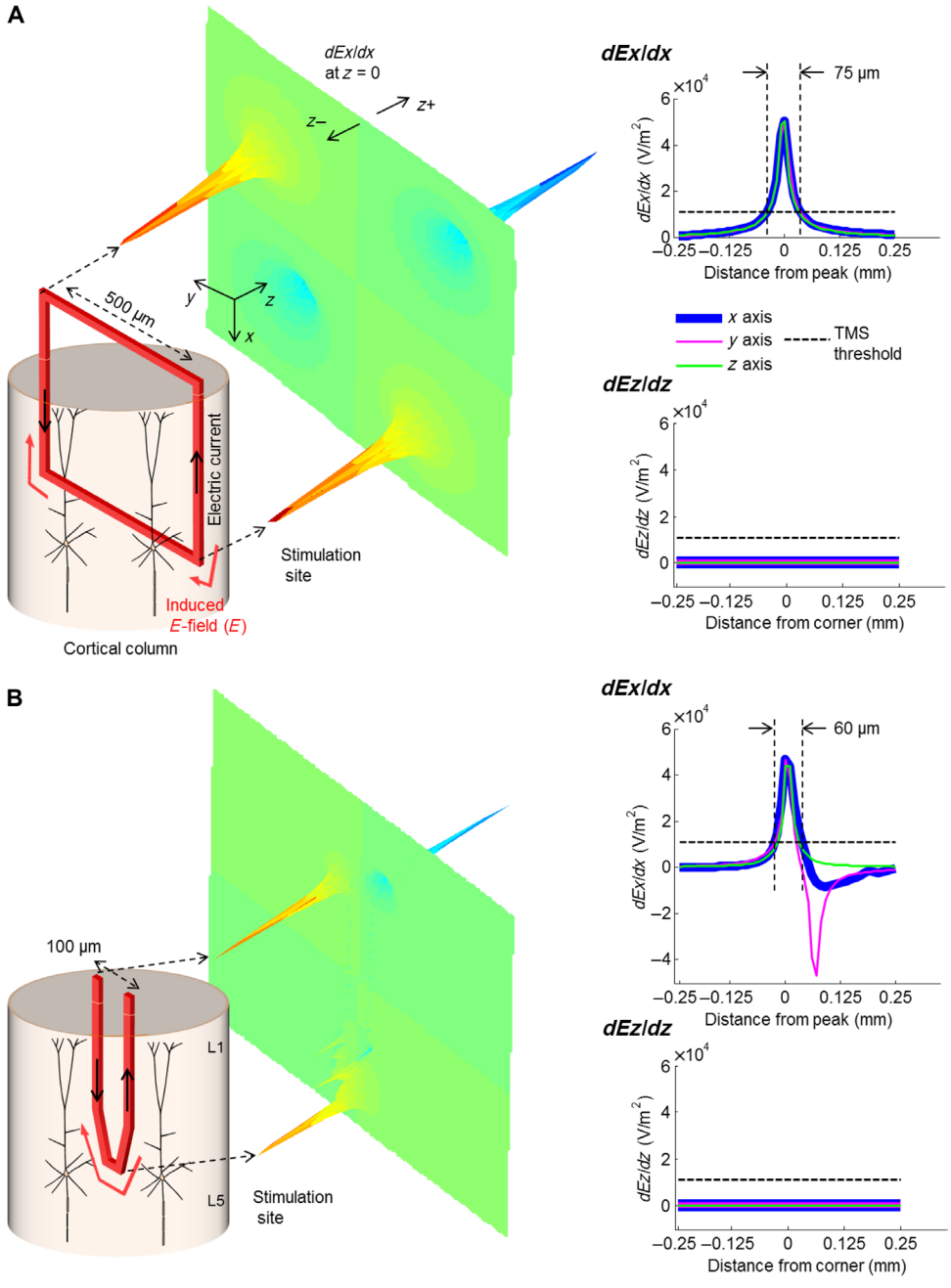

Fig. 1. Micrometer-sized microcoils generate suprathreshold fields. (**A**) Surface (middle) plot of the electric field gradients in the *x* direction (*dEx*/*dx*) arising from the 500-µm square coil on the left (red). Note that the horizontally oriented peaks in the surface plot indicate the peak gradients in a direction normal to the cortical surface, that is, up and down in the cortical column representation on the left. Right: Two-dimensional profile of the gradients in the vertical (*dEx*/*dx*, top) and horizontal (*dEz*/*dz*, bottom) directions; the "0" on the abscissa corresponds to the bottom right corner of the coil. The horizontal lines indicate estimated threshold levels from earlier studies with much larger coils (see text). Dashed vertical lines indicate the width of the suprathreshold region. (**B**) Similar to (A), except for a 100-µm trapezoidal coil.

was also constructed by carefully bending a 50-µm-diameter copper wire (Fig. 3B). Although this second coil did not have as sharp a bend as the microfabricated coil, the thicker cross-sectional area of the wire allowed stronger currents. Five-micrometer polyurethane/polyamide insulation prevented the leakage of electrical current from this second coil into the bath or tissue. Its resistance was ~13 ohms.

Fabricated microcoils were first tested for their ability to activate cortical neurons during in vitro experiments using coronal brain slices from mice (Materials and Methods; Fig. 3, C to K). A loose-seal cell-attached patch-clamp electrode was positioned on the soma of a targeted layer 5 (L5) PN within the whisker (motor) cortex and used to record action potentials elicited by magnetic stimulation from the microcoil (Materials and Methods). Patch-clamp recordings have proven effective for allowing visualization of elicited action potentials in previous studies with electric stimulation because the amplifiers are not saturated by the stimulus; for example, the electrical artifact associated with the stimulus does not preclude observation of neuronal responses (*24*, *25*). The coil was positioned close to the targeted cell

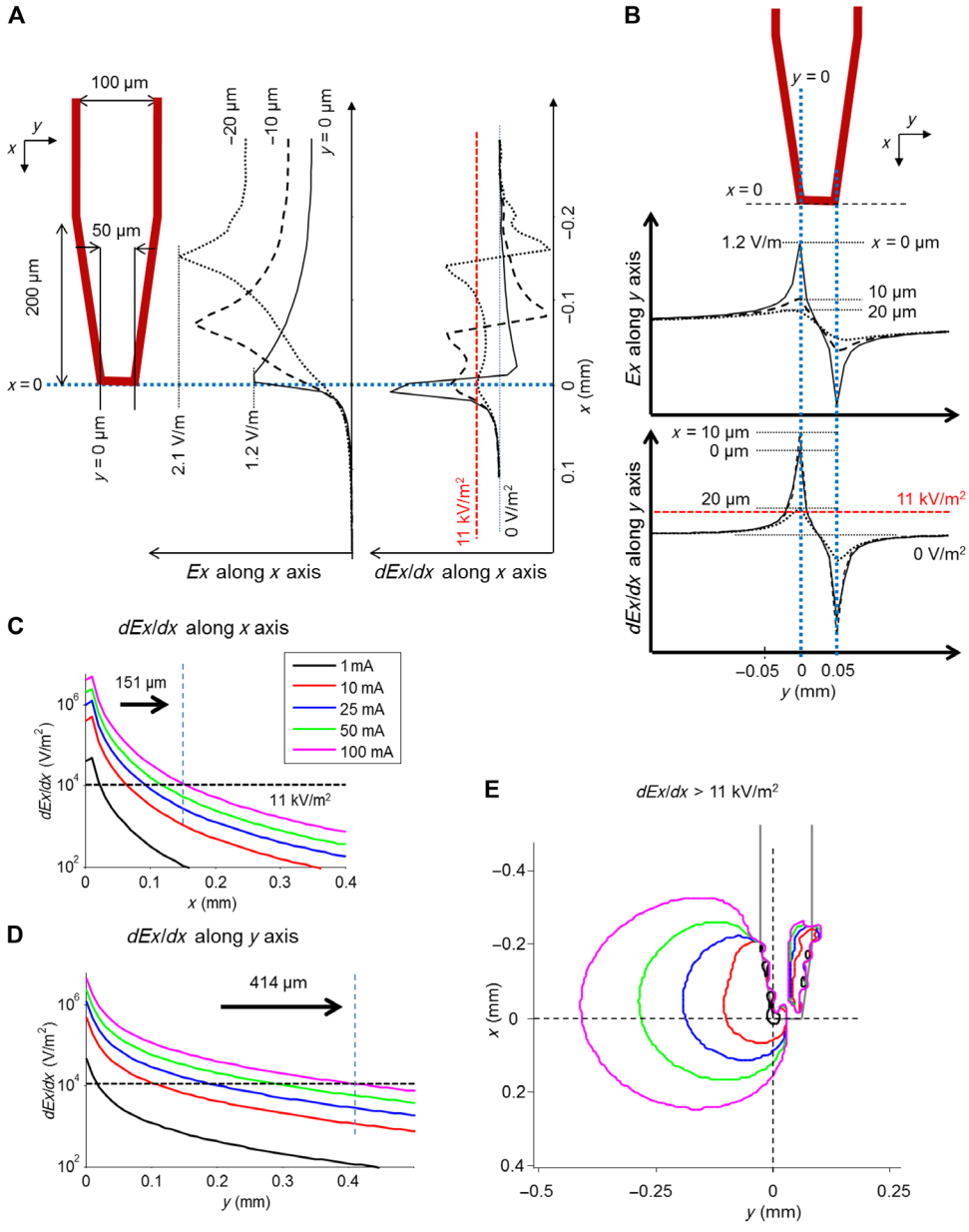

Fig. 2. Area of suprathreshold field expands as current amplitude increases. (**A**) Plots of the electric fields (middle) and the field gradients (right) arising from the microcoil (left) in the *x* direction (*dEx/dx*) along the *x* axis for three different vertical cross sections through the coil. The red dashed lines in the gradient plot indicate estimated threshold levels from earlier studies with transcranial magnetic stimulation coils (see text). (**B**) Plots of the electric fields (middle) and the spatial gradients (bottom) in the *x* direction (*dEx/dx*) along the *y* axis for three horizontal cross sections. (**C**) Extracted portion of the field gradient profiles for different amplitudes along the *x* axis for values of $x \geq 0$. (**D**) Similar to (C), but for the field gradients along the *y* axis for values of $y \leq 0$. (**E**) Contour plots of suprathreshold gradient areas for different current amplitudes.

with the tip centered over the proximal axon, the portion of the cell that was thought to have the highest sensitivity to stimulation (*26*, *27*). To ensure that observed responses arose from direct activation of the cell itself, that is, not secondary to activation of one or more presynaptic neurons, we added 10 µM 2,3-dihydroxy-6-nitro-7-sulfamoyl-benzo[f] quinoxaline (NBQX), 10 µM bicuculline, and 50 µM D-2-amino-5-phosphonopentanoic acid (D-APV) to the perfusion bath in some experiments to block synaptic input to the cell. Stimulation at relatively low amplitude levels produced an electrical artifact that consisted of a short-duration biphasic waveform that persisted for ~0.4 ms (Fig. 3C, top left). Increasing the amplitude of stimulation slightly produced a similar artifact but now continued into a more prolonged waveform (Fig. 3C, top right). The addition of 1 µM tetrodotoxin (TTX) to the bath eliminated the prolonged part of the response (Fig. 3C, bottom right, red trace), suggesting that it was an action potential, and subtraction of the response in TTX from the corresponding control response revealed a waveform (blue trace) that was highly similar to those action potentials that arose spontaneously. Elicited action potentials could also be extracted from the raw recordings (without the use of TTX) by subtracting responses that contained the artifact only from those that contained an artifact plus an action potential (Fig. 3D, black); this process revealed a waveform that again had amplitude and kinetics

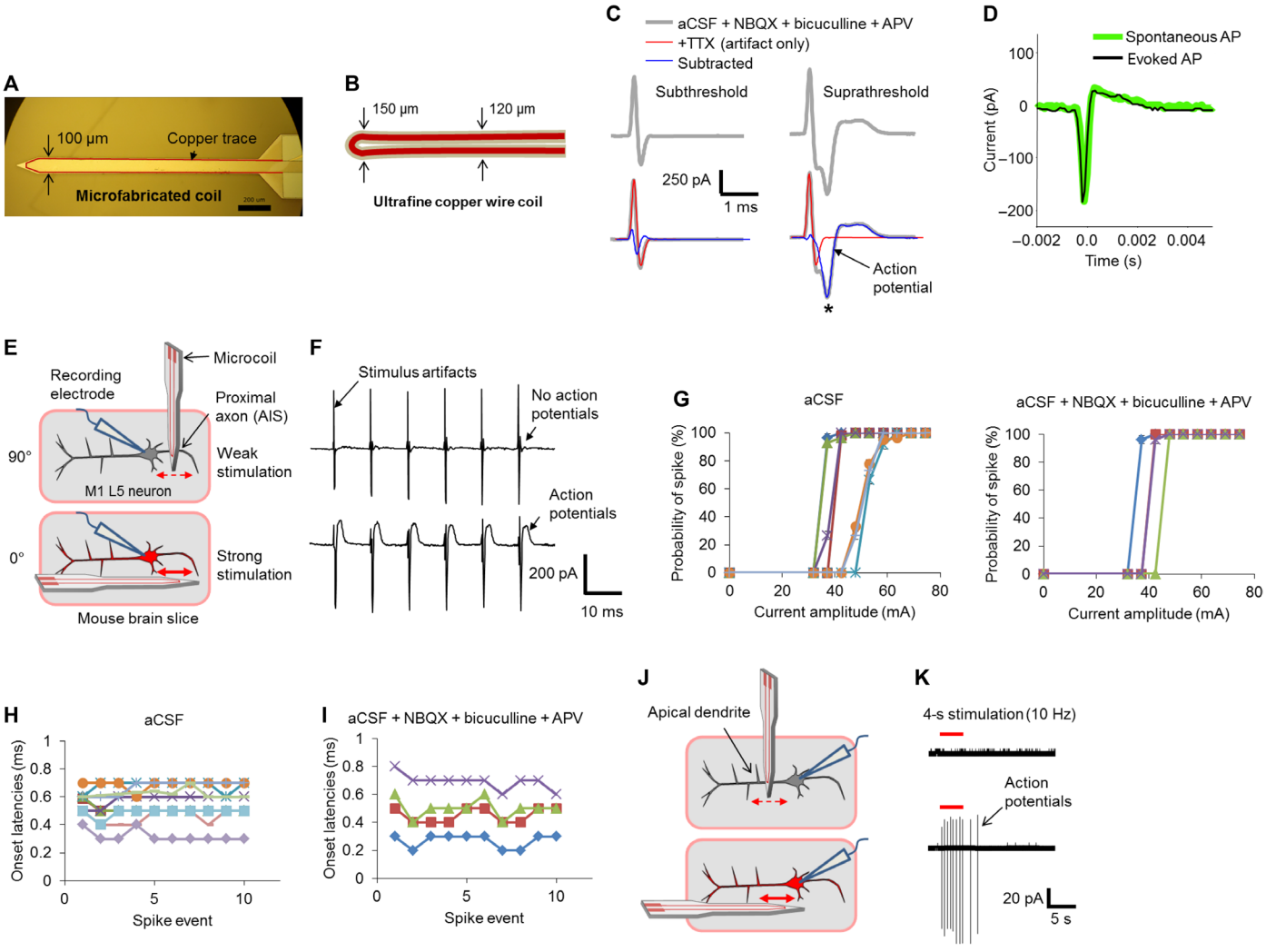

Fig. 3. Microcoils activate cortical PNs in vitro. (**A**) Schematic of the microfabricated coil consisting of a copper trace (red) on a silicon substrate (yellow). (**B**) Illustration of the bent-wire microcoil. The 50-µm copper wire (red) is surrounded by 5-µm polyurethane/polyamide insulation. (**C**) Responses to subthreshold (left) and suprathreshold stimulation (right) in the presence of synaptic blockers (top traces) and with TTX added (bottom traces). The blue curves were computed by subtracting the TTX traces from the corresponding traces in the top panels. The asterisk indicates the evoked action potential. (**D**) Action potentials (APs) could also be extracted without the use of TTX by subtracting a response without a presumed spike (artifact only) from a response with a spike; the black trace is such a spike [different cell from (C)]. A spontaneous spike from the same cell is overlaid (green). (**E**) Schematic of the in vitro experimental setup. A cell-attached patch electrode was used to record from the soma of an L5 PN in response to stimulation from the microcoil; the long axis of the coil could be positioned either normal to (top) or parallel to the slice surface (bottom). In all cases, the tip of the coil was positioned over the proximal axon. The red dashed and solid horizontal arrows represent weak and strong (respectively) electric fields induced along the length of the axon. AIS, axon initial segment. (**F**) Typical responses for each orientation. Stimulation was delivered at a rate of 100 Hz; the stimulus artifact indicates the timing of each pulse. The prominent after-hyperpolarizations seen following each pulse in the bottom traces are reliable indicators of elicited spikes. (**G**) Probability of eliciting an action potential as a function of stimulation current amplitude for control artificial cerebrospinal fluid (aCSF) (left, $n = 7$ cells) and with synaptic blockers added (right, $n = 4$ cells). (**H**) Onset latencies of evoked spikes were plotted for 10 consecutive pulses delivered at 100 Hz in 11 individual neurons. All spikes were elicited within 0.3 to 0.7 ms after onset of the stimulus. (**I**) Same as (H), but with synaptic blockers added to the perfusion bath ($n = 4$ cells). (**J**) Schematic of the experimental setup showing the coil positioned over the apical dendrites in either a perpendicular (top) or a parallel orientation (bottom). (**K**) Typical responses to apical dendrite stimulation for each orientation. The red horizontal bar indicates the duration over which stimulation was applied.

that were nearly identical to those from a spontaneous action potential (Fig. 3D, green trace). This suggests that the direct subtraction method for identifying action potentials is comparably effective to the use of TTX. Together, these experiments indicate that magnetic stimulation from microcoils can elicit action potentials through direct activation of L5 PNs.

To explore the ability of the coils to selectively target neurons, we ran experiments in which the orientation of the coil was varied relative to the orientation of the targeted PN. Initially, the plane of the coil was held perpendicular to the surface of the slice (Fig. 3E, top), resulting in a weak electric field and gradient along the length of the neuron. As expected, this configuration was not effective (Fig. 3F, top), even for the strongest amplitude that could be delivered by our system. The coil was then reoriented with its flat surface approximately parallel to the slice surface (Fig. 3E, bottom); this orientation is similar to that which would arise during insertion of the microcoil into the intact cortex and

resulted in a strong gradient along the length of the neuron that led to robust spiking (Fig. 3F, bottom); note that the presence of the positive-going after-hyperpolarization that closely follows each stimulus provides a clear marker for the presence of an elicited action potential (*24*). With direct activation, individual stimuli could each induce a single action potential at even the fastest rates tested (up to 100 Hz; $n = 11$ of 11; Fig. 3F, bottom). Similar to electric stimulation, stronger levels of magnetic stimulation increased the likelihood that a given pulse would elicit a spike (Fig. 3G, left; $n = 7$) and revealed thresholds of 44.21 ± 7.31 mA (SD) for direct activation. The sensitivity to stimulation in these cells was not significantly affected by the addition of synaptic blockers to the perfusion bath (Fig. 3G, right; $n = 4$). The ability to extract and visualize individual spikes also allowed the timing of individual spikes to be precisely determined and revealed onset latencies of ≤1.0 ms (Fig. 3H). As expected from spikes that are directly activated, latencies were not sensitive to the addition of synaptic blockers (Fig. 3I).

Repositioning the coil such that its tip was over the apical dendrite of the targeted neuron (Fig. 3J) allowed the sensitivity of this portion of the neuron to be explored as well. Once again, orienting the plane of the coil perpendicular to the slice surface (Fig. 3J, top) resulted in very weak electric fields along the neuron and did not produce spiking (Fig. 3K, top). However, alignment of the coil parallel to the surface of the slice (Fig. 3J, bottom) produced robust spiking ($n = 8$; Fig. 3K, bottom). The onset latencies of spikes elicited by stimulation over the apical dendrite were not well correlated to individual stimuli and were typically ≥3 ms, suggesting that spikes were mediated through the activation of the surrounding neural network. The addition of pharmacological blockers of excitatory synaptic input to the perfusion bath [10 μM CNQX (6-cyano-7-nitroquinoxalene-2,3-dione) and 50 μM D-APV] eliminated these responses, thereby confirming their presynaptic origin. The thresholds for indirect activation were 46.50 ± 11.78 mA (SD), and therefore both modes of activation had similar thresholds. Consistent with previous electric stimulation studies (*6*, *28*, *29*), it was not possible to elicit an individual action potential for each stimulus via indirect activation, even at the highest stimulus amplitudes. We did not attempt to identify the specific presynaptic neuron(s) activated by stimulation over the apical dendrite, but the high sensitivity of L5 PNs to vertically oriented electric fields raises the possibility that another vertically oriented neuron is activated; L2/3 PNs are an obvious possibility, especially because they are known to make excitatory synapses to L5 PNs. It is, of course, possible that multiple neuronal types are activated by stimulation from the microcoil, and further testing will be required to identify the specific types activated as well as to elucidate the subsequent synaptic interactions that occur.

For direct activation, thresholds were generally lowest when the tip of the coil was situated over the proximal axon at a distance of ~50 μm from the soma. Previous studies with electric stimulation have shown that the threshold for direct activation is minimized when the electrode is precisely centered over the dense band of sodium channels within the spike initiation zone of the proximal axon (*26*, *30*), and it is likely that the lowest thresholds here arise because of the proximity to this location. However, we did not typically expend the considerable time and effort required to determine the exact location at which threshold is minimized (*26*), and so the 44.21-mA value reported here may not represent the absolute minimum threshold that can be obtained. For indirect activation, thresholds were generally lowest when the coil was over the apical dendrite at a distance of ~200 μm from the soma, although once again we did not systematically attempt to find the location for which threshold was minimized. Despite the fact that the values obtained here do not necessarily represent the absolute minimum thresholds, the levels that are reported here are still considerably lower than those reported with the previous microcoil for in vitro activation (*13*, *19*). For example, previous work with the original microcoil (inductor) required thresholds of 717 mA for activation (*13*), whereas the thresholds for in vitro activation here were 44.21 mA (~16× reduction; see fig. S1 for further comparison of power levels). The lower threshold levels that were observed here likely arose because the smaller size of the coil not only generated stronger fields but also allowed for closer proximity to targeted neurons. Note also that for the responses that arose through indirect activation (Fig. 3K, bottom), the electrical artifact arising from the stimulus was quite small. This is consistent with the spatially narrow extent of the induced electric fields (Fig. 2) versus the relatively large separation between the coil and the recording electrode. Minimization of the stimulus artifact is a highly attractive feature, especially for efforts in which it is essential to record the response to artificial stimulation (*31*).

To better explore the spatial extent of magnetic stimulation as well as its ability to selectively activate specific orientations, we ran an additional series of experiments using brain slices from GCaMP6 mice (Materials and Methods). Cortical PNs from these animals express a calcium indicator that increases its level of fluorescence in response to spiking; similar to previous reports (*32*, *33*), we observed low levels of fluorescence in the somas of individual L5 PNs (Fig. 4, A and C). Before measuring the responses to magnetic stimulation, we first examined the responses that arose from electric stimulation delivered via a conventional implantable electrode (Materials and Methods). At low levels of stimulation, there was little change in fluorescence, but as the amplitude of stimulation increased, the region over which fluorescence increased became progressively larger (Fig. 4B); this is consistent with results from previous studies of electric stimulation in vivo (*6*). At the highest level of stimulation tested here, a 200 μm × 200 μm region of the slice was strongly activated and uniformly extended in all directions. Similar to electric stimulation, low levels of magnetic stimulation also produced little change in the level of fluorescence, and higher levels resulted in increasing areas of activation (Fig. 4D). However, the spatial extent of activation was more narrowly confined with magnetic stimulation, and the location over which cells were activated was consistent with the predictions that arose from computational modeling (Figs. 2 and 4F). Although the responses shown in Fig. 4 (B and D) reflect the fluorescence of both somas and the surrounding neuropils (that is, axons and dendrites), the analysis could also be restricted to evaluate fluorescence changes in somas only (*6*, *32*, *33*). For the strongest stimulus tested here (52 mA), somas up to a distance of 160 μm from the coil exhibited robust increases ($\Delta F/F > 5$ to 10%) in fluorescence (Fig. 4E), whereas smaller increases ($\Delta F/F > 1$ to 3%) in fluorescence were exhibited by cells even further away. Thus, consistent with the modeling predictions of Fig. 2E, magnetic stimulation from these coils can modulate activity well beyond the region over which encapsulation and cell migration are expected to occur (*11*, *22*, *34*, *35*), thereby suggesting that these coils can remain viable during chronic implantation.

To eliminate the possibility that nonmagnetic factors contributed to the spiking responses observed here, we performed a series of control experiments, similar to the ones performed with the larger microcoil in earlier studies (*13*, *19*). For example, the integrity of the coil insulation was tested regularly by measuring the impedance to ground; values were

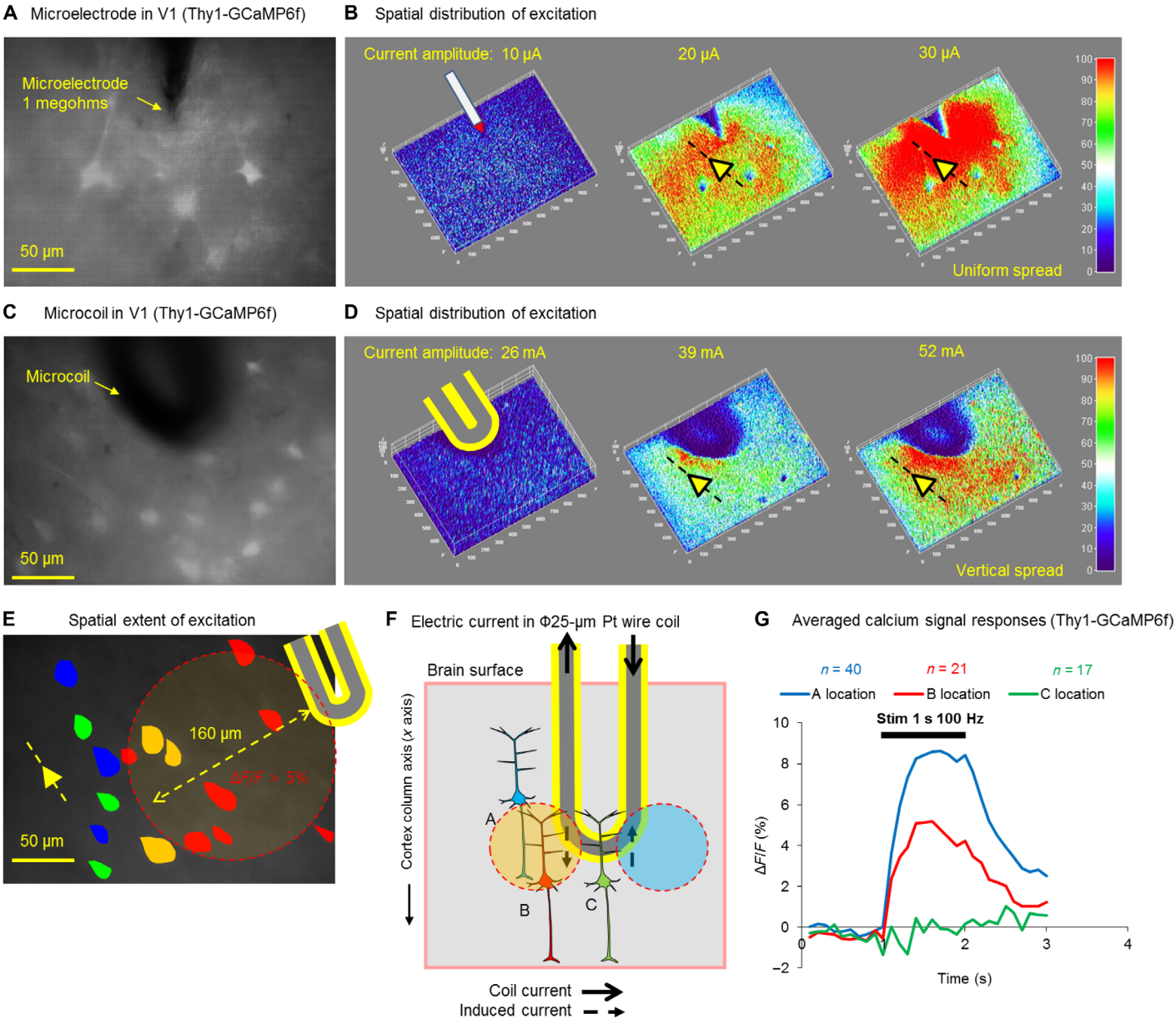

Fig. 4. Comparison of spatial extent of excitation. (**A**) Light microscope photograph of a microelectrode situated over a V1 coronal slice from Thy1-GCaMP6f transgenic mice. The somas of individual neurons from L5 can be observed. (**B**) The change in fluorescence in response to three different levels of stimulation from an electrode. The tip of the electrode is seen as a downward-pointing triangle at the top of each image. The yellow triangle and the dashed line indicate the approximate orientation of cortical columns. (**C**) Similar to (A), showing the microcoil implanted over the V1 slice. The approximately semicircular tip of the coil is seen at the top of the image. (**D**) The change in fluorescence in response to three different levels of magnetic stimulation. (**E**) A region of interest (ROI) was defined for individual PNs on the basis of the somatic outline and used to calculate the cellular calcium fluorescence transients in each cell. Red neurons show strong calcium transients ($\Delta F/F$ >5%); yellow and green neurons indicate moderate ($\Delta F/F$ > 3%) and weak calcium transients ($\Delta F/F$ > 1%), respectively. Blue neurons indicate no observable increase in calcium fluorescence. (**F**) Schematic diagram illustrating the region over which PNs are predicted to be activated by stimulation from the coil. The proximal axon of PNs at location A (blue soma) is aligned with the region for which the induced field gradient (along the length of the neuron) is suprathreshold (yellow circular region); the apical dendrites of other neurons (location B, red soma) also extend into the suprathreshold region and become activated as well; and the processes of neurons that do not extend into the strong gradient region (location C, green soma) do not become activated. (**G**) Average calcium transient responses for the L5 PNs depicted in (F).

typically ~1 gigohm and were always greater than 200 megohms, thereby eliminating the possibility of direct electric stimulation contributing to observed responses. We also monitored the temperature in the bath as well as in the surrounding brain tissue during magnetic stimulation and observed increases of less than 1°C, well below the threshold for thermal activation of neurons (*36*–*38*). Capacitive currents can be transmitted through the coil insulation and have previously been shown to be effective for neuronal activation (*39*). However, there was no return electrode in the recording chamber in our experiments, and hence currents were not "forced" through the tissue as they were in a previous study (*39*). Although this greatly reduces the potential likelihood of capacitive activation, we nevertheless ran a control experiment in which a

large transient current was used to "burn" a small portion of the coil, thereby leaving an open circuit; the transient current was not strong enough to also burn through the surrounding insulation, and thus there remained no potential for direct electrical activation. The subsequent delivery of stimulation to the "broken" coil produced a voltage differential across the open circuit, essentially acting as a capacitor. However, this approach was not effective for eliciting neural activity and therefore suggests that the observed responses were not mediated through capacitive activation. Finally, to eliminate the possibility that one or more (noncoil) hardware elements from our experimental setup might be generating the fields that are responsible for neuronal activation, care was taken to leave all hardware components in a fixed position across all experiments. In this manner, the only component that was not spatially fixed across trials was the orientation of the coil relative to targeted cells. Because some experiments induced neuronal responses whereas others did not, it is unlikely that any of the noncoil hardware components contributed meaningfully to activation, and we conclude that the fields arising from an appropriately oriented microcoil were the primary source of activation.

In vivo animal experiments

On the basis of the successful activation of PNs in vitro, we implanted the new coils into the whisker (motor) cortex of anesthetized mice to explore whether they could also drive neuronal circuits in vivo. Following a craniotomy and removal of the dura (Materials and Methods), both coil designs (Fig. 3, A and B) could be easily inserted into the cortex (n = 18 and 6, respectively). There was no evidence of excessive bleeding or other complications during the ensuing experiments (with durations of up to 2 hours). Coil tips were inserted to a depth of approximately 500 μm, aligning the tip to the highly sensitive proximal axon of L5 PNs and using the coil orientation that was most effective with the in vitro experiments (Fig. 3C, bottom). The whisker cortex was an attractive target to evaluate in vivo efficacy because it allowed direct comparisons of results to many earlier studies with implanted electrodes (*40*–*42*). For example, analogous to the results with electric stimulation, the direction of whisker movement was similarly sensitive to the frequency of magnetic stimulation: 10-Hz stimulation of the whisker motor cortex in the left hemisphere (5 pulses; Fig. 5A, left) reliably produced protraction of the whiskers on the right side (Fig. 5B, top right, upward deflections; n = 8 of 8), whereas 100-Hz stimulation (10 pulses; Fig. 5A, right) caused retraction (Fig. 5B, bottom right, downward deflections; n = 8 of 8). Also similar to electric stimulation responses, the onset of whisker protraction in response to magnetic stimulation was slower than the onset of whisker retraction (Fig. 5E; n = 5; t test, P = 0.0008). Although elicited movements in the anesthetized animal were small, they were comparable in magnitude to those elicited previously in anesthetized animals with electric stimulation (*40*, *42*). In some cases, we observed larger deflections as the anesthesia started to wear off, although we did not attempt to quantify these differences. Qualitatively similar results were obtained with both coils.

To confirm that implantable coils were also effective for activating the sensory cortex, we also inserted coils into the barrel cortex (Fig. 5C, left) and again examined the whisker movements evoked by magnetic stimulation (Fig. 5, C and D). Both 10- and 100-Hz stimulation caused whisker retraction only (Fig. 5C, right panels; n = 5 of 5), consistent with the movements elicited by electric stimulation (*41*). Together, these results provide strong evidence that the new microcoils can effectively drive neuronal circuits in vivo. Further, the strong parallels of the responses induced here by magnetic stimulation to the responses described previously with electric stimulation suggest that similar patterns of neural activity are elicited by each.

The thresholds for in vivo activation were 7 to 10 mA and were therefore approximately one-fifth of those associated with in vitro activation. Once again, we did not systematically evaluate thresholds as a function of the depth of insertion nor did we seek to determine whether significantly shallower depths, for example, those that would position the coil tip over the apical dendrite, would be more effective. Thus, further reductions in threshold may be possible. In general, the thresholds associated with the fabricated coils were slightly less than those made from bent wires. However, we are hesitant to draw too strong a conclusion here because the different coil designs may have biased placement of one of the designs to a more sensitive portion of the neuron.

Low-power repetitive micromagnetic stimulation

Previous experiments with electric stimulation have demonstrated that neuronal responses can be elicited by repetitive delivery of low-amplitude stimuli, even when each stimulus by itself is subthreshold. As an example, hippocampal neurons can be activated by field strengths of 0.14 V/m from stimuli delivered at 1 to 2 Hz (*43*), although the threshold for activation of Purkinje and stellate neurons with a single pulse is thought to be close to 10 V/m (*44*). A similar finding with magnetic stimulation would be potentially attractive because it might help to further reduce the power consumption associated with these devices. We tested whether whisker movements could be evoked by repetitive stimulation at rates ranging from 1 to 100 Hz while the amplitude was held fixed at the lowest level we could deliver (11.2 mV, corresponding to a stimulus current of 0.75 mA). For a rate of 1 Hz, a single pulse was delivered every second for a total duration of 10 s, whereas for all other rates (10, 50, and 100 Hz), three pulses were delivered every second for a duration of 5 s (the timing of different stimulus trains is depicted in Fig. 6A). Low-amplitude stimulation induced small whisker movements (Fig. 6B) that, similar to earlier experiments, reversed direction for higher rates of stimulation (Fig. 6, B and C) (n = 8 of 8). We quantified the level of movement by averaging the amplitude of whisker deflections during stimulation and comparing it to the deflections that arose before and after stimulation [Fig. 6C, averaged for 2 s before and 10 s after stimulation (see Materials and Methods); n = 5; t test, P = 0.0001]. The results reveal small but statistically significant movements that were induced by these stimuli. Although the long latencies associated with these responses will need to be overcome for this type of approach to be practically useful, the results are nevertheless encouraging because they suggest that activation may be possible at very low power levels.

DISCUSSION

Here, we showed that a new microcoil, comparable in size to electrodes that are routinely implanted into the cortex, can effectively activate neurons in vitro and also drive neural circuits in vivo. By using a single sharp bend of a thin wire, a strong, local electric field gradient that was well in excess of previous estimates of activation threshold could be generated. This new design allowed the cross-sectional profile of the implant to be reduced from 500 μm × 500 μm in the original inductor to a 50 μm × 100 μm profile here; the smaller size allowed coils to be safely inserted into the cortex instead of restricting placement to noncortical regions as with previous microcoil designs (*23*).

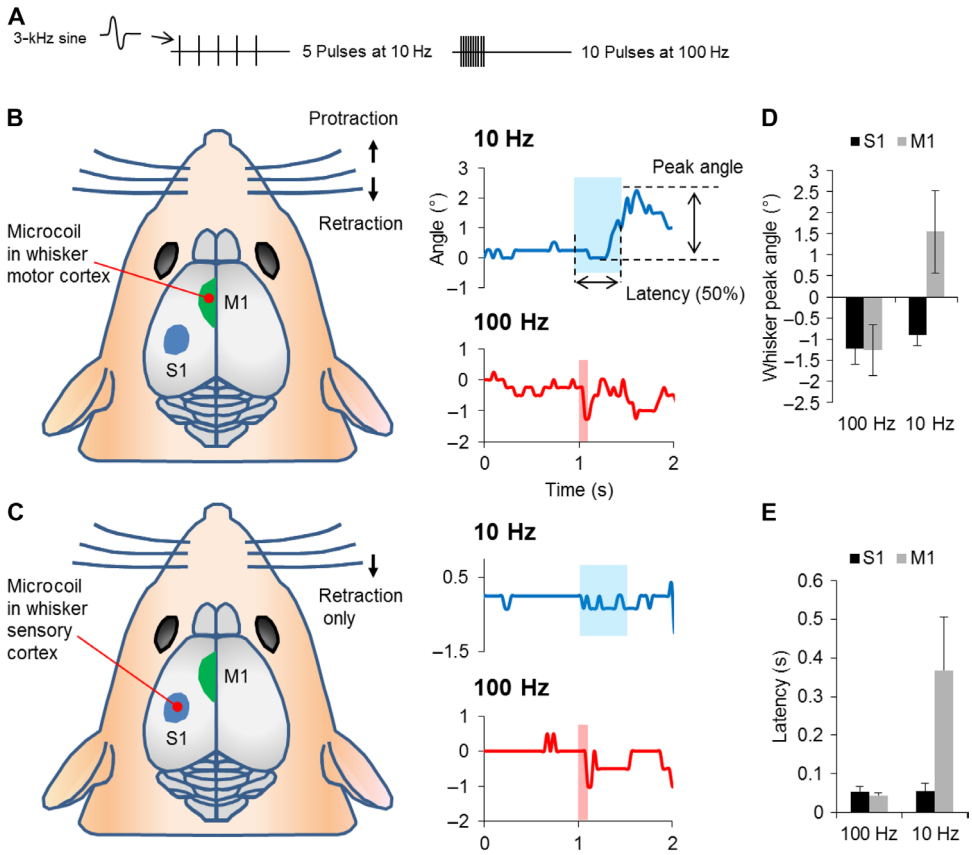

Fig. 5. Implanted microcoils activate neuronal circuits in vivo. (**A**) Stimulus waveforms consisted of 5 pulses delivered at 10 Hz or 10 pulses delivered at 100 Hz. Each pulse consisted of one full period of a 3-kHz sinusoid with an amplitude of 112 mV. (**B**) Left: Coils were inserted into the whisker motor cortex (left hemisphere). Ten-hertz stimulation resulted in protraction of whiskers (upward deflections) on the right side (top), whereas 100-Hz stimulation induced retraction (downward deflections) (bottom). (**C**) Illustration of the approximate location for coil insertion to simulate the whisker sensory cortex. Both 10- and 100-Hz stimulation resulted in whisker retraction (top and bottom panels on the right). (**D**) Mean amplitudes of peak whisker movements for each stimulus condition. (**E**) Mean latency for the onset of whisker movements for each stimulus condition.

Physiological testing confirmed model predictions and showed not only that microcoil stimulation can activate cortical neurons but also that specific types of neurons can be selectively targeted. For example, in vitro experiments showed strong activation when the induced electric field was aligned along the length of the targeted PN but little or no activation when the coil was rotated by 90°, for example, so that the electric field and its gradient were orthogonal to the targeted neuron. Similar to electric stimulation, even prolonged stimulation at high amplitudes was not effective for this orientation. This suggests that when the coil was inserted into the cortex for in vivo experiments, horizontally oriented passing axons were subjected to minimal activation force and likely remained unresponsive, whereas local PNs were strongly activated. It has been shown that incidental activation of passing axons by electric stimulation causes the response to a given stimulus to spread well beyond the local region surrounding the electrode (*6*–*8*). The spread of activation is undesirable because it reduces the effectiveness of stimulation; for example, both the potential acuity that can be achieved with a prosthesis that targets the visual cortex and the ability of a brain-computer interface to provide precise feedback signals to the primary somatosensory cortex are diminished. Thus, the ability of coil-based magnetic stimulation to activate vertically oriented PNs without simultaneously activating horizontally oriented passing axons may help to better confine activation to only local neurons and may lead to more effective stimulation. Further testing will be required to establish whether other, nonpyramidal, vertically oriented neurons or axons are also activated by coils and to determine the relative sensitivity of each. Despite the uncertainty in identifying the underlying mechanism of activation, the strong similarities in behavioral responses to magnetic versus electric stimulation suggest that the underlying neuronal responses may be similar for the two modalities.

Analogous to the use of electric stimulation, the volume of neurons activated by microcoils could be altered by changes to the amplitude of stimulation as well as by the design of the coil itself. At low stimulus amplitudes, activation could be confined to those neurons within ~60 μm of the coil tip. This translates to a volume of ~0.0001 mm^3; using a previous estimate of neuronal density in mouse M1 [74,775 cells/mm^3 (*45*)] results in activation of eight cells with the 1-mA stimulus. For comparison, the volume of tissue activated by a 50-mA stimulus was estimated to be 0.009 mm^3, resulting in activation of 676 cells.

We also estimated the volume of activation in our in vitro experiments by systematically stepping the coil away from a targeted cell at a given stimulus strength. These experiments led to qualitatively similar values to those estimated from the model; for example, the 50-mA stimulus remained effective within a distance of ~150 μm to

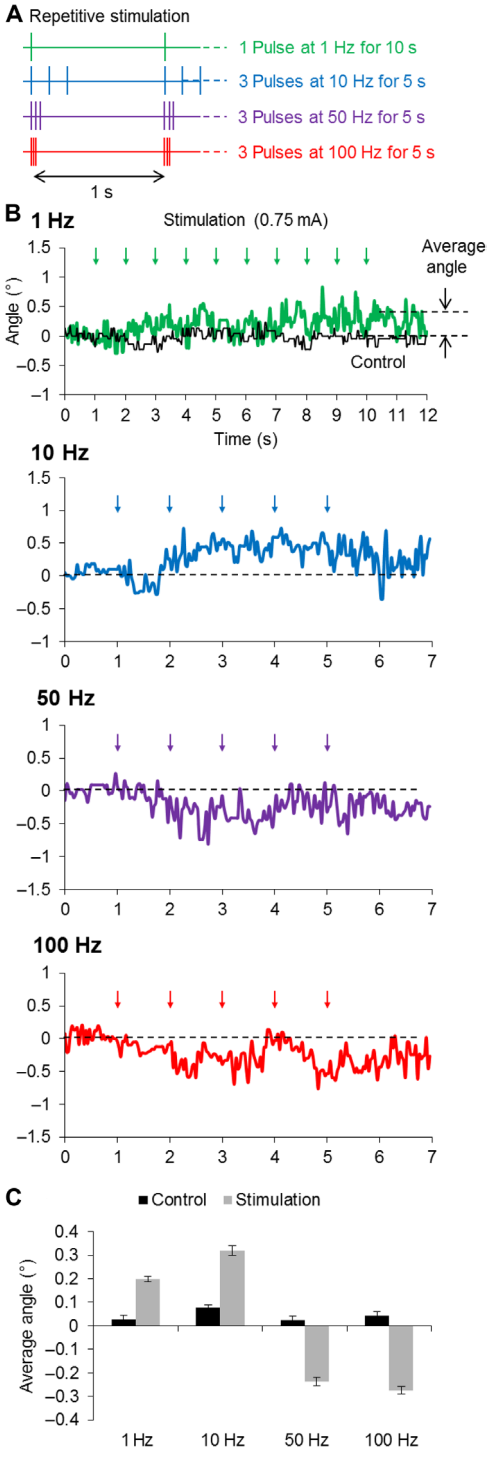

Fig. 6. Continuous stimulation induces whisker movement at reduced power levels. (**A**) Schematic illustration of the repetitive stimulation waveforms. Each "pulse" was a single 3-kHz sinusoid. (**B**) Averaged whisker movement in response to repetitive stimulation at power levels of 11.2 mV (0.75 mA). (**C**) Average whisker movements for each waveform (upward denotes protraction; downward indicates retraction).

the cell—approximately the same as that predicted by the model. Further confirmation of this estimate comes from the calcium imaging experiments; for example, the zone of activation extended ~160 μm from the coil for a 52-mA stimulus. This ability to extend the region of activation will be important for chronic implants given the prevalence of glial scarring that can surround implants (*11*, *12*) as well as the potential for migration of cells away from the implant (*22*, *35*). The properties of the induced electric fields from coils may remain more consistent over time because magnetic fields pass readily through the high-impedance glial encapsulation that can surround implants although encapsulation can markedly alter the strength as well as the spatial distribution of the electric fields arising from electrodes. In addition, the lack of direct metal-to-brain contact for coils eliminates many of the electrode-brain interface problems, for example, the variability of electrode impedance following implantation (*9*, *15*).

The results of this study suggest that power consumption, defined as the product of current-squared and impedance, will not preclude the use of microcoils in acute or chronic studies. The current levels associated with magnetic stimulation are typically higher than those associated with electric stimulation, whereas the impedance of coils is typically many orders of magnitude lower (for example, 20 ohms versus 1 megohm). Thus, to a first approximation, the currents required for coils can be two to three orders of magnitude greater than those from electrodes but still result in a similar level of power consumption. Of course, many additional factors influence power usage, and higher current levels may require specialized power supplies, but this estimate suggests that the higher levels of current will not necessarily result in excessive power levels.

The new coil design was associated with a considerable reduction in thresholds (power levels are summarized in fig. S1). For example, the threshold for single-pulse activation of L5 PNs in brain slices was 40 to 45 mA, nearly 16× lower than the thresholds obtained in analogous experiments with the original coil. This translates to a reduction in power from ~2 W to ~10 mW. Thresholds for in vivo activation with the new coil were even lower (7 to 10 mA) and brought estimated power levels down to 0.4 mW, a reduction of more than two orders of magnitude from those required in previous in vivo experiments with the original microcoil (*13*). It is almost certain that a large portion of the reduction in in vivo thresholds arises from the ability to insert the new design directly into the cortex, whereas the previous design restricted coil placement to the cortical surface.

Although the estimates here are still preliminary, it is nevertheless encouraging that they compare favorably to the levels for existing clinical devices; for example, power levels for deep brain stimulation implants range from 2 to 24.5 mW (fig. S1). Power levels from the new microcoils also compare favorably to those associated with electric stimulation of the motor cortex in vivo [0.5 mW (*40*)]. However, coil-based power levels still exceed those from electric stimulation of the sensory cortex (0.002 to 0.05 mW). Some of this difference may reflect a higher sensitivity of the sensory cortex versus that of the motor cortex (*46*–*49*), and thus further testing in visual cortical neurons may lead to further reductions in power. Regardless, the power levels associated with stimulation from microcoils have dropped several orders of magnitude since the introduction of the original coil and are likely to drop further given the rapid evolution of this technology.

In addition to reducing power levels, it is likely that the size and selectivity of microcoils will continue to be further optimized. Even

relatively simple enhancements, such as incorporating multiple sharp-bend wires at the same location, are likely to enhance the strength of stimulation. Other design enhancements, such as the use of multiple wires at different depths within the same probe shank, may allow selective targeting of neurons at different depths; for example, those PNs of L2/3 and of L5 could each be activated independently. This approach might help to better re-create physiological signaling patterns with a prosthesis. It is also likely that the relatively simple bends that were used here can be enhanced to further optimize both the efficacy of stimulation and the orientation selectivity, that is, double bends in the tip (forming a "w" shape) may prove to be even more selective than the simple bends that were used here. The use of materials that enhance magnetic field strength (for example, ferrite, mu-metal, and permalloy) may also help to further increase the efficacy of stimulation with a corresponding reduction in power levels. Finally, the use of nanometer-scale wires may help to further reduce coil size without a significant loss in efficacy. The combination of selective targeting, increased reliability, and power levels that are comparable to or maybe even less than those of existing devices raises the possibility that implanted microcoils may provide a highly attractive alternative to existing electrode-based approaches for cortical stimulation.

MATERIALS AND METHODS

Modeling of microcoils

Custom software, written in MATLAB, was used to calculate the spatial gradient of induced electric fields (*E*-fields) that arose from the flow of current through a microcoil (*13*, *19*).

From Faraday's laws, the *E*-field, $\vec{E}$, is related to the time-varying magnetic field by

$$\nabla \times \vec{E} = -\frac{\partial \vec{B}}{\partial t} \tag{1}$$

Because the magnetic field, $\vec{B}$, can be obtained by taking the curl of the magnetic vector potential, $\vec{A}$ (that is, $\vec{B} = \nabla \times \vec{A}$), the equation for *E*-field can be expressed as

$$\vec{E} = -\frac{\partial \vec{A}}{\partial t} - \nabla V \tag{2}$$

Under the assumptions that there is no charge on the coil and that the current distribution in the coil is uniform (that is, quasi-static condition), ∇V is equal to 0 and Eq. 2 becomes

$$\vec{E} = -\frac{\partial \vec{A}}{\partial t} \tag{3}$$

The magnetic vector potential is calculated from the coil geometry as follows

$$\vec{A} = \frac{\mu_0 N i}{4\pi} \cdot \oint \frac{dl}{R} \tag{4}$$

where μ_0 is the permeability constant, *N* is the number of turns, *i* is the electric current through the coil, *R* is the vector between the coil segment and the target segment at which the *E*-field is calculated, and *dl* is the small segment of the coil.

Because the principal axis of the PNs within each cortical column was approximately parallel to the *x* axis (compare Fig. 1), the *E*-field along the cortical column can be calculated by numerical integration along the length of the coil loop.

$$\partial \vec{E}_x = -\frac{\mu_0 N \left(\frac{di}{dt}\right)}{4\pi} \cdot \oint \frac{1}{R} dl_x \tag{5}$$

where the *x* dimension corresponds to the long axis of the PN.

Integrating $\partial \vec{E}_x$ with respect to the *x* component of the line gives the following equation for $\vec{E}_x$

$$\vec{E}_x = -\frac{\mu_0 N \left(\frac{di}{dt}\right)}{4\pi} \cdot \ln\left[x - x_0 + \sqrt{(x-x_0)^2 + (y-y_0)^2 + (z-z_0)^2}\right]_{x_1}^{x_2} \tag{6}$$

In the above equation, the coil element lies at (x_0,y_0,z_0) and the *E*-field is calculated at (x,y,z). x_1 and x_2 represent the positions of the corners of the rectangular coil in the *x* axis. The spatial gradient, $\frac{\partial \vec{E}_x}{\partial x}$, is calculated by taking the derivative of the analytical solution for $\vec{E}_x$ from Eq. 6. The input current to the coil, *i* , was a half-period of a 3-kHz sinusoidal waveform with an amplitude of 1 mA (*13*, *19*).

Two types of microcoils were considered and modeled. The first type was a square loop (500 μm per side) that was essentially a single loop extracted from the inductor used in previous studies (Fig. 1A) (*13*). The second type was an asymmetric trapezoid-shaped loop that was 1000 μm long and 100 μm wide; the width tapered down to 50 μm at the tip (Fig. 1B). The trapezoid-shaped loop coil was highly similar to the silicon microprobe coil that was used in subsequent physiological experiments.

Fabrication and testing of microcoils

The microcoil fabrication process was based on silicon processing techniques. First, a 50-μm-thick, 4-inch-diameter silicon wafer was bonded to a handling wafer with an adhesive. Subsequently, a 100- to 200-nm-thick SiO_2 layer was deposited using plasma-enhanced chemical vapor deposition (PECVD). Then, a 2-μm-thick copper layer was sputtered using electron beam (e-beam)–assisted physical vapor deposition with a 10-nm-thin titanium layer to improve adhesion. Next, a photoresist, used as a mask for the next etching step, was spin-coated and baked. The photoresist was patterned by exposure to ultraviolet light through a phase-shifting photomask. After that, the copper was wet-etched using a solution of Transene Copper Etchant 49-1. The photoresist was stripped off in acetone, and then 300 nm of insulating SiO_2 was deposited on top using PECVD. The area of the electrical contact pads was shadowed to ensure that it was free of the top insulation. Following this step, a photoresist, used as the mask in the silicon etch, was spin-coated and patterned. The 50-μm-thick silicon substrate was etched through using deep reactive ion etching. The resulting microcoil structures (Fig. 3A) were then released from the handling wafer in acetone and dried. We also made a microcoil using an ultrafine copper wire [50-μm bare diameter (45-AWG), polyurethane base coat, polyamide overcoat, 60 μm with insulation; Essex] (Fig. 3B).

The fabricated coils were assembled with copper wire leads (34-AWG, polyurethane inner coat and nylon overcoat) (Belden). The electrical contacts of the microcoils were connected to the copper wire leads using a silver conductive epoxy (CircuitWorks Conductive Epoxy, ITW Chemtronics). Assembled coils were mounted on a custom-made plastic holder with an instant adhesive, and the distal ends of the copper wire leads were attached to the signal and ground leads of a BNC (Bayonet Neill–Concelman) connector. The custom-made assemblies were secured to the micromanipulator of a stereotaxic frame (Model 900, David Kopf Instruments) for accurate positioning over the mouse cortex.

Each microcoil assembly was tested both before and after each experiment to ensure that there was no leakage of electrical current from the coil into the mouse cortex (*19*). Coils were submerged in physiological solution (0.9% NaCl), and the impedance between one of the coil terminals and an electrode immersed in the physiological solution was measured before and after each in vivo animal experiment. Impedances above 200 megohms were considered indicative of adequate insulation. The high impedance ensured that direct electrical currents did not contribute to any of the elicited neural activity underlying observed mouse behaviors.

Micromagnetic stimulation drive

The output of a function generator (AFG3021B, Tektronix Inc.) was connected to a 1000-W audio amplifier (PB717X, Pyramid Inc.) with a gain of 5.6 V/V and a bandwidth of 70 kHz. The audio amplifier was powered by a battery (LC-R1233P, Panasonic Corp.). The output of the amplifier was monitored with an oscilloscope (TDS2014C, Tektronix Inc.). A stimulation pulse consisted of a single full-period 3-kHz sinusoid waveform. The amplitude of sinusoids from the function generator ranged from 0 to 200 mV. The output of the amplifier for sinusoids was 0 to 1.12 V. Single-burst stimulation (Fig. 5A) consisting of 5 or 10 pulses was delivered at 10 and 100 Hz, respectively. Repetitive stimulation at 1 pulse/s was delivered for a total of 10 s. Other repetitive stimulations consisted of 3 pulses/s at 10, 50, or 100 Hz for a total duration of 5 s.

In vitro brain slice experiments

Electrophysiological recordings were performed using brain slices prepared from 17- to 30-day-old mice (C57BL/6J; The Jackson Laboratory). The care and use of animals followed all federal and institutional guidelines, the Institutional Animal Care and Use Committees of the Boston Veterans Affairs (VA) Healthcare System, and the Subcommittee on Research Animal Care of the Massachusetts General Hospital. The mice were deeply anesthetized with isoflurane and decapitated. The brains were removed immediately after death, and a section of the brain containing the whisker M1 (0.5 to 1 mm anterior to the bregma) was isolated on ice in a 0° to 5°C oxygenated solution containing 1.25 mM NaH_2PO_4, 2.5 mM KCl, 25 mM $NaHCO_3$, 1 mM $MgCl_2$, 25 mM glucose, and 225 mM sucrose, equilibrated with 95% O_2–5% CO_2 (pH 7.4). This cold solution, with a low sodium ion and without calcium ion content, improved tissue viability. In the same medium, 300- to 400-μm-thick coronal slices were prepared using a vibrating blade microtome (Vibratome 3000 Plus, Ted Pella Inc.) and were incubated at room temperature in an aCSF solution containing 125 mM NaCl, 1.25 mM NaH_2PO_4, 2.5 mM KCl, 25 mM $NaHCO_3$, 1 mM $MgCl_2$, 2 mM $CaCl_2$, and 25 mM glucose, equilibrated with 95% O_2–5% CO_2 (pH 7.4). After a 2-hour recovery period, slices that contained M1 were transferred and mounted, caudal side down, to a plastic recording chamber (RC-27L, Warner Instruments, LLC) with a plastic slice anchor (SHD-27LP/2, Warner Instruments, LLC). The chamber was maintained at 30° ± 2°C and continuously superfused (3.3 ml/min) with oxygenated aCSF solution.

Whisker M1 L5 PNs were targeted under visual control. Spiking was recorded with a patch electrode (4 to 8 megohms) that was filled with superfusate and positioned onto the surface of a targeted PN [a loose-seal (15- to 20-megohm) cell-attached mode]. The patch-clamp amplifier was a MultiClamp 700B Amplifier (Molecular Devices) operated in voltage-clamp mode with a holding potential (that is, command potential) of 0 mV or similar levels at which the amplifier current I_{amp} is 0 pA. Recording somatic action potentials in this mode is thought to capture the capacitive charging current ($Cm{\cdot}dV/dt$), and so waveforms reflect the derivative of voltage over time instead of voltage versus time but nevertheless provide an accurate indicator of somatic spiking (*24*, *50*–*54*). The use of voltage-clamp mode results in the capture of the currents underlying the action potential and therefore depolarizations are reflected by downward deflections (inward currents), followed by upward, hyperpolarizing currents. Two silver chloride–coated wires served as the ground and were positioned at opposite edges of the recording chamber, each approximately 15 mm from the targeted cell. The microcoil assembly was fixed in the micromanipulator such that the plane of the coil was held either perpendicular or parallel to the top surface of the slice (compare Fig. 3E). The coil assembly was lowered into the bath until the coil was 50 μm above the targeted PN.

In some experiments, 10 μM CNQX (or 10 μM NBQX) and/or 50 μM D-AP5 or D-APV was added to the perfusion bath to block AMPA/kainate and NMDA (*N*-methyl-D-aspartate) channels, respectively. Both drugs were purchased from Sigma-Aldrich Corp. The $GABA_A$ (γ-aminobutyric acid type A) receptor antagonist (+)-bicuculline (10 μM; Tocris Bioscience) was used to block inhibitory synaptic transmission. TTX (1 μM; EMD Millipore Corp.) was used to block action potentials. Drugs were prepared daily from concentrated stock solutions; deionized water was added to dilute stock solutions to the appropriate concentration shortly before application.

Calcium fluorescence imaging and analysis

Calcium fluorescence imaging was performed using brain slices prepared from 17- to 30-day-old transgenic mice (Thy1-GCaMP6f; The Jackson Laboratory). The care and use of animals followed all federal and institutional guidelines, the Institutional Animal Care and Use Committees of the Boston VA Healthcare System, and the Subcommittee on Research Animal Care of the Massachusetts General Hospital. The brain slices were prepared and maintained using the same methods described above and were then incubated in a dark room at room temperature in the aCSF solution. After a 2-hour recovery period, slices that contained the primary visual cortex (V1) were transferred and mounted, caudal side down, to the plastic recording chamber (RC-27L) with a plastic slice anchor (SHD-27LP/2).

Imaging was performed with a Nikon Eclipse FN1 microscope (Nikon Instruments Inc.) through a 20× 0.5 numerical aperture objective (Nikon Fluor 20× /0.50 water immersion objective). The excitation light source (X-Cite 120Q; Excelitas Technologies Corp.) was coupled to the epifluorescent port of the microscope. Calcium fluorescence changes were captured with a charge-coupled device camera (DFK 31BU03.H; USB 2.0 color industrial camera; 1024 × 768 pixels; 30 frames/s; The Imaging Source, LLC). The actual imaging area was 267 μm × 200 μm.

Calcium fluorescence transients in V1 L5 PNs were first evoked by electrical stimulations with 200-μs, 0- to 30-μA cathodic first

biphasic current pulses (that is, 100 pulses were delivered at a repetition rate of 100 Hz) through a 1-megohm platinum-iridium (Pt-Ir) microelectrode (Microprobes for Life Science) positioned in L4 or L5 (Fig. 4, A and B). Each electric stimulus was delivered three to five times, and calcium transients from each trial were averaged.

Microcoils were then positioned in L4 or L5, and calcium fluorescence transients were evoked by magnetic stimulations with a single period of a sinusoidal waveform; the input current amplitude ranged from 0 to 74 mA. One hundred pulses were typically delivered at a repetition rate of 100 Hz. Microcoils were made of 25-μm-diameter Pt-Ir wires with 4-μm-thick polytetrafluoroethylene insulation (A-M Systems) (Fig. 4, C and D). Magnetic stimulation was repeated three to five times, and calcium transients were averaged to determine the response.

Images were recorded using image capture software (IC Capture; The Imaging Source, LLC) and processed using image analysis software (ImageJ; National Institutes of Health). Calcium fluorescence transients for individual PNs were extracted using methods described previously (*32*, *33*). Briefly, outlines of individual PNs were defined to create ROIs, and the cellular calcium transients were calculated by averaging the pixels within each ROI. Calcium transients for neuropil within a 20-μm annular-shaped region surrounding each neuron were also extracted for correction of neuropil contamination (*33*). True fluorescence transients from a neuron (cell body) were estimated using the following equation: $F_{cell\_true}(t) = F_{cell\_apparent}(t) - r \times F_{surrounding\_neuropil}(t)$, where t is the time and r is the contamination ratio [$r = 0.7$ was chosen for the 20× objective in this study (*32*, *33*)]. After the neuropil correction, the calcium fluorescence transients for individual neurons were calculated as $\Delta F/F\ (\%) = (F - F_0)/F_0$, where F_0 was the baseline fluorescence level calculated by averaging over 2 s before the onset of stimulation.

In vivo animal experiments

All experiments were performed using mice that were 2 to 4 months old (C57BL/6J; The Jackson Laboratory). The care and use of animals followed all federal and institutional guidelines, the Institutional Animal Care and Use Committees of the Boston VA Healthcare System, and the Subcommittee on Research Animal Care of the Massachusetts General Hospital. Mice were deeply anesthetized with a cocktail of ketamine hydrochloride (100 mg/kg intraperitoneal injection) and xylazine (10 mg/kg intraperitoneal injection) before the start of surgery. Additional ketamine ($^1/_{10}$ initial dose) was supplemented every 30 min to maintain the plane of anesthesia.

Anesthetized mice were placed into a stereotaxic frame (David Kopf Instruments) for the craniotomy as well as all subsequent testing. A heating blanket on the floor of the frame was used to maintain body temperature at 37°C (rectally monitored). Lidocaine (2 mg/kg, subcutaneously) was injected into the scalp, and a midline incision was made, followed by removal of the portion of the skull and dura overlying the motor cortex and/or the sensory cortex. Microcoils were implanted into the whisker motor cortex (0.5 to 1 mm anterior and 0.2 mm lateral to the bregma) or into the whisker sensory cortex (1 to 2 mm posterior and 2 mm lateral to the bregma). Coils were inserted to a depth of 500 μm unless otherwise specified.

Detection of whisker movements in anesthetized mice

We videotaped the whisker movements that arose in response to magnetic stimulation using a high-definition web camera (LifeCam HD-5000; Microsoft) so that quantification of movements could be accurately determined. All the video files were captured at a rate of 30 frames/s, sufficient to detect the relatively slow whisker movements. Video recording of the whisker movements started 2 s before the onset of stimulation and ended 12 s after the end of stimulation. Whisker movements for the 2-s period before the onset of stimulation and the 2-s period that occurred 10 to 12 s after the termination of the stimulus were used to calculate baseline (control) movements. Stimulation generally evoked rhythmic whisker movements that persisted for 3 to 5 s after the termination of the stimulus. Whisker trajectories were generated from the raw video files using motion tracking and analysis software (Kinovea, www.kinovea.org). Three or five repetitions were averaged for each stimulation parameter.

Data analysis

In all statistical analyses, unpaired t tests were used to assess whether the difference between the average values for different stimulation conditions was significant. Differences associated with P values <0.05 were regarded as statistically significant. Variances are reported as ±SD or ±SE.

SUPPLEMENTARY MATERIALS

Supplementary material for this article is available at http://advances.sciencemag.org/cgi/content/full/2/12/e1600889/DC1

fig. S1. Power consumption levels for microcoils and other stimulation modalities.

References (*55*–*58*)

REFERENCES AND NOTES

1. S. J. Bensmaia, L. E. Miller, Restoring sensorimotor function through intracortical interfaces: Progress and looming challenges. *Nat. Rev. Neurosci.* **15**, 313–325 (2014).
2. E. M. Schmidt, M. J. Bak, F. T. Hambrecht, C. V. Kufta, D. K. O'Rourke, P. Vallabhanath, Feasibility of a visual prosthesis for the blind based on intracortical microstimulation of the visual cortex. *Brain* **119**, 507–522 (1996).
3. R. A. Normann, B. A. Greger, P. House, S. F. Romero, F. Pelayo, E. Fernandez, Toward the development of a cortically based visual neuroprosthesis. *J. Neural Eng.* **6**, 035001 (2009).
4. R. A. Andersen, E. J. Hwang, G. H. Mulliken, Cognitive neural prosthetics. *Annu. Rev. Psychol.* **61**, 169–190 (2010).
5. J. B. Ranck Jr., Which elements are excited in electrical stimulation of mammalian central nervous system: A review. *Brain Res.* **98**, 417–440 (1975).
6. M. H. Histed, V. Bonin, R. C. Reid, Direct activation of sparse, distributed populations of cortical neurons by electrical microstimulation. *Neuron* **63**, 508–522 (2009).
7. M. R. Behrend, A. K. Ahuja, M. S. Humayun, R. H. Chow, J. D. Weiland, Resolution of the epiretinal prosthesis is not limited by electrode size. *IEEE Trans. Neural Syst. Rehabil. Eng.* **19**, 436–442 (2011).
8. A. C. Weitz, D. Nanduri, M. R. Behrend, A. Gonzalez-Calle, R. J. Greenberg, M. S. Humayun, R. H. Chow, J. D. Weiland, Improving the spatial resolution of epiretinal implants by increasing stimulus pulse duration. *Sci. Transl. Med.* **7**, 318ra203 (2015).
9. T. S. Davis, R. A. Parker, P. A. House, E. Bagley, S. Wendelken, R. A. Normann, B. Greger, Spatial and temporal characteristics of V1 microstimulation during chronic implantation of a microelectrode array in a behaving macaque. *J. Neural Eng.* **9**, 065003 (2012).
10. A. Koivuniemi, S. J. Wilks, A. J. Woolley, K. J. Otto, Multimodal, longitudinal assessment of intracortical microstimulation. *Prog. Brain Res.* **194**, 131–144 (2011).
11. V. S. Polikov, P. A. Tresco, W. M. Reichert, Response of brain tissue to chronically implanted neural electrodes. *J. Neurosci. Methods* **148**, 1–18 (2005).
12. W. M. Grill, S. E. Norman, R. V. Bellamkonda, Implanted neural interfaces: Biochallenges and engineered solutions. *Annu. Rev. Biomed. Eng.* **11**, 1–24 (2009).
13. G. Bonmassar, S. W. Lee, D. K. Freeman, M. Polasek, S. I. Fried, J. T. Gale, Microscopic magnetic stimulation of neural tissue. *Nat. Commun.* **3**, 921 (2012).
14. S. W. Lee, S. I. Fried, The response of L5 pyramidal neurons of the PFC to magnetic stimulation from a micro-coil. *Conf. Proc. IEEE Eng. Med. Biol. Soc.* **2014**, 6125–6128 (2014).
15. S. F. Cogan, Neural stimulation and recording electrodes. *Annu. Rev. Biomed. Eng.* **10**, 275–309 (2008).

16. S. F. Cogan, K. A. Ludwig, C. G. Welle, P. Takmakov, Tissue damage thresholds during therapeutic electrical stimulation. *J. Neural Eng.* **13**, 021001 (2016).
17. T. Saxena, L. Karumbaiah, E. A. Gaupp, R. Patkar, K. Patil, M. Betancur, G. B. Stanley, R. V. Bellamkonda, The impact of chronic blood–Brain barrier breach on intracortical electrode function. *Biomaterials* **34**, 4703–4713 (2013).
18. A. Canales, X. Jia, U. P. Froriep, R. A. Koppes, C. M. Tringides, J. Selvidge, C. Lu, C. Hou, L. Wei, Y. Fink, P. Anikeeva, Multifunctional fibers for simultaneous optical, electrical and chemical interrogation of neural circuits in vivo. *Nat. Biotechnol.* **33**, 277–284 (2015).
19. S. W. Lee, S. I. Fried, Suppression of subthalamic nucleus activity by micromagnetic stimulation. *IEEE Trans. Neural Syst. Rehabil. Eng.* **23**, 116–127 (2015).
20. F. Rattay, The basic mechanism for the electrical stimulation of the nervous system. *Neuroscience* **89**, 335–346 (1999).
21. P. J. Maccabee, V. E. Amassian, L. P. Eberle, R. Q. Cracco, Magnetic coil stimulation of straight and bent amphibian and mammalian peripheral nerve in vitro: Locus of excitation. *J. Physiol.* **460**, 201–219 (1993).
22. D. McCreery, V. Pikov, P. R. Troyk, Neuronal loss due to prolonged controlled-current stimulation with chronically implanted microelectrodes in the cat cerebral cortex. *J. Neural Eng.* **7**, 036005 (2010).
23. H.-J. Park, G. Bonmassar, J. A. Kaltenbach, A. G. Machado, N. F. Manzoor, J. T. Gale, Activation of the central nervous system induced by micro-magnetic stimulation. *Nat. Commun.* **4**, 2463 (2013).
24. S. I. Fried, H. A. Hsueh, F. S. Werblin, A method for generating precise temporal patterns of retinal spiking using prosthetic stimulation. *J. Neurophysiol.* **95**, 970–978 (2006).
25. S. W. Lee, D. K. Eddington, S. I. Fried, Responses to pulsatile subretinal electric stimulation: Effects of amplitude and duration. *J. Neurophysiol.* **109**, 1954–1968 (2013).
26. S. I. Fried, A. C. W. Lasker, N. J. Desai, D. K. Eddington, J. F. Rizzo III, Axonal sodium-channel bands shape the response to electric stimulation in retinal ganglion cells. *J. Neurophysiol.* **101**, 1972–1987 (2009).
27. E. J. Tehovnik, W. M. Slocum, Electrical induction of vision. *Neurosci. Biobehav. Rev.* **37**, 803–818 (2013).
28. B. Gustafsson, E. Jankowska, Direct and indirect activation of nerve cells by electrical pulses applied extracellularly. *J. Physiol.* **258**, 33 (1976).
29. S. D. Stoney Jr., W. D. Thompson, H. Asanuma, Excitation of pyramidal tract cells by intracortical microstimulation: Effective extent of stimulating current. *J. Neurophysiol.* **31**, 659–669 (1968).
30. E. J. Tehovnik, A. S. Tolias, F. Sultan, W. M. Slocum, N. K. Logothetis, Direct and indirect activation of cortical neurons by electrical microstimulation. *J. Neurophysiol.* **96**, 512–521 (2006).
31. V. Gilja, C. A. Chestek, I. Diester, J. M. Henderson, K. Deisseroth, K. V. Shenoy, Challenges and opportunities for next-generation intracortically based neural prostheses. *IEEE Trans. Biomed. Eng.* **58**, 1891–1899 (2011).
32. T.-W. Chen, T. J. Wardill, Y. Sun, S. R. Pulver, S. L. Renninger, A. Baohan, E. R. Schreiter, R. A. Kerr, M. B. Orger, V. Jayaraman, L. L. Looger, K. Svoboda, D. S. Kim, Ultrasensitive fluorescent proteins for imaging neuronal activity. *Nature* **499**, 295–300 (2013).
33. A. M. Kerlin, M. L. Andermann, V. K. Berezovskii, R. C. Reid, Broadly tuned response properties of diverse inhibitory neuron subtypes in mouse visual cortex. *Neuron* **67**, 858–871 (2010).
34. J. P. Seymour, D. R. Kipke, Neural probe design for reduced tissue encapsulation in CNS. *Biomaterials* **28**, 3594–3607 (2007).
35. Y. Zhong, R. V. Bellamkonda, Dexamethasone-coated neural probes elicit attenuated inflammatory response and neuronal loss compared to uncoated neural probes. *Brain Res.* **1148**, 15–27 (2007).
36. R. Chen, G. Romero, M. G. Christiansen, A. Mohr, P. Anikeeva, Wireless magnetothermal deep brain stimulation. *Science* **347**, 1477–1480 (2015).
37. J. L. Carvalho-de-Souza, J. S. Treger, B. Dang, S. B. H. Kent, D. R. Pepperberg, F. Bezanilla, Photosensitivity of neurons enabled by cell-targeted gold nanoparticles. *Neuron* **86**, 207–217 (2015).
38. K. Eom, C. Im, S. Hwang, S. Eom, T. S. Kim, H. S. Jeong, K. H. Kim, K. M. Byun, S. B. Jun, S. J. Kim, Synergistic combination of near-infrared irradiation and targeted gold nanoheaters for enhanced photothermal neural stimulation. *Biomed. Opt. Express* **7**, 1614–1625 (2016).
39. M. Eickenscheidt, M. Jenkner, R. Thewes, P. Fromherz, G. Zeck, Electrical stimulation of retinal neurons in epiretinal and subretinal configuration using a multicapacitor array. *J. Neurophysiol.* **107**, 2742–2755 (2012).
40. M. Brecht, M. Schneider, B. Sakmann, T. W. Margrie, Whisker movements evoked by stimulation of single pyramidal cells in rat motor cortex. *Nature* **427**, 704–710 (2004).
41. F. Matyas, V. Sreenivasan, F. Marbach, C. Wacongne, B. Barsy, C. Mateo, R. Aronoff, C. C. H. Petersen, Motor control by sensory cortex. *Science* **330**, 1240–1243 (2010).
42. M. Brecht, A. Krauss, S. Muhammad, L. Sinai-Esfahani, S. Bellanca, T. W. Margrie, Organization of rat vibrissa motor cortex and adjacent areas according to cytoarchitectonics, microstimulation, and intracellular stimulation of identified cells. *J. Comp. Neurol.* **479**, 360–373 (2004).
43. J. T. Francis, B. J. Gluckman, S. J. Schiff, Sensitivity of neurons to weak electric fields. *J. Neurosci.* **23**, 7255–7261 (2003).
44. C. Y. Chan, C. Nicholson, Modulation by applied electric fields of Purkinje and stellate cell activity in the isolated turtle cerebellum. *J. Physiol.* **371**, 89–114 (1986).
45. S. Herculano-Houzel, C. Watson, G. Paxinos, Distribution of neurons in functional areas of the mouse cerebral cortex reveals quantitatively different cortical zones. *Front. Neuroanat.* **7**, 35 (2013).
46. M. Jazayeri, Z. Lindbloom-Brown, G. D. Horwitz, Saccadic eye movements evoked by optogenetic activation of primate V1. *Nat. Neurosci.* **15**, 1368–1370 (2012).
47. I. Diester, M. T. Kaufman, M. Mogri, R. Pashaie, W. Goo, O. Yizhar, C. Ramakrishnan, K. Deisseroth, K. V. Shenoy, An optogenetic toolbox designed for primates. *Nat. Neurosci.* **14**, 387–397 (2011).
48. D. K. Murphey, J. H. R. Maunsell, Electrical microstimulation thresholds for behavioral detection and saccades in monkey frontal eye fields. *Proc. Natl. Acad. Sci. U.S.A.* **105**, 7315–7320 (2008).
49. M. H. Histed, A. M. Ni, J. H. R. Maunsell, Insights into cortical mechanisms of behavior from microstimulation experiments. *Prog. Neurobiol.* **103**, 115–130 (2013).
50. K. L. Perkins, Cell-attached voltage-clamp and current-clamp recording and stimulation techniques in brain slices. *J. Neurosci. Methods* **154**, 1–18 (2006).
51. S. I. Fried, T. A. Münch, F. S. Werblin, Mechanisms and circuitry underlying directional selectivity in the retina. *Nature* **420**, 411–414 (2002).
52. C. Cai, P. Twyford, S. Fried, The response of retinal neurons to high-frequency stimulation. *J. Neural Eng.* **10**, 036009 (2013).
53. J. F. Atherton, D. L. Wokosin, S. Ramanathan, M. D. Bevan, Autonomous initiation and propagation of action potentials in neurons of the subthalamic nucleus. *J. Physiol.* **586**, 5679–5700 (2008).
54. C. J. Wilson, M. D. Bevan, Intrinsic dynamics and synaptic inputs control the activity patterns of subthalamic nucleus neurons in health and in Parkinson's disease. *Neuroscience* **198**, 54–68 (2011).
55. A. M. Kuncel, W. M. Grill, Selection of stimulus parameters for deep brain stimulation. *Clin. Neurophysiol* **115**, 2431–2441 (2004).
56. E. J. Tehovnik, W. M. Slocum, Depth-dependent detection of microampere currents delivered to monkey V1. *Eur. J. Neurosci.* **29**, 1477–1489 (2009).
57. E. A. DeYoe, J. D. Lewine, R. W. Doty, Laminar variation in threshold for detection of electrical excitation of striate cortex by macaques. *J. Neurophysiol.* **94**, 3443–3450 (2005).
58. H. Tischler, S. Wolfus, A. Friedman, E. Perel, T. Pashut, M. Lavidor, A. Korngreena, Y. Yeshurun, I. Bar-Gad, Mini-coil for magnetic stimulation in the behaving primate. *J. Neurosci. Methods* **194**, 242–251 (2011).

Acknowledgments

Funding: This work was supported by the Veterans Administration–Rehabilitation Research and Development Service (1I01RX001663), the National Eye Institute (R01-EY023651), the National Institute for Neurological Disease and Stroke (U01-NS099700), and the Rappaport Foundation. **Author contributions:** S.W.L. and S.I.F. conceived this study. S.W.L. designed the implantable microcoils and performed the computational modeling. B.D.F.C. and F.F. designed and built the microfabricated prototype, with input from S.W.L. and S.I.F. S.W.L. fabricated the ultrafine wire microcoils, built all coil assemblies, and performed the animal experiments. S.W.L. and S.I.F. analyzed the results, wrote the manuscript, and prepared the figures. **Competing interests:** The authors declare that they have no competing interests. **Data and materials availability:** All data needed to evaluate the conclusions in the paper are present in the paper and/or the Supplementary Materials. Additional data related to this paper may be requested from the authors.

Submitted 25 April 2016
Accepted 3 November 2016
Published 9 December 2016
10.1126/sciadv.1600889

Citation: S. W. Lee, F. Fallegger, B. D. F. Casse, S. I. Fried, Implantable microcoils for intracortical magnetic stimulation. *Sci. Adv.* **2**, e1600889 (2016).